ELSEVIER

Contents lists available at ScienceDirect

Biosensors and Bioelectronics

journal homepage: www.elsevier.com/locate/bios





ECoGScope: An integrated platform for real-time Electrophysiology and fluorescence imaging

Jonghee Eun^{a,#}, Jeongseop Kim^{a,#}, Tae-Eun Kim^{a,b}, Ja Wook Koo^{a,b,**}, Namsun Chou^{a,1,*}

ARTICLE INFO

Keywords:
Multimodal neural interfaces
Microendoscope
Fluorescence imaging
Electrocorticography (ECoG) electrode array
Mesh electrode
Polydimethylsiloxane (PDMS)

ABSTRACT

In this study, we present ECoGScope, a versatile neural interface platform designed to integrate multiple functions for advancing neural network research. ECoGScope combines an electrocorticography (ECoG) electrode array with a commercial microendoscope, enabling simultaneous recording of ECoG signals and fluorescence imaging. The electrode array, constructed from highly flexible and transparent polymers, ensures conformal contact with the brain surface, allowing unobstructed optical monitoring of neural activity alongside electrophysiological recordings. A key innovation is the compact connection module, which securely integrates the ECoG array and microendoscope while minimizing interference with animal behavior. The device was successfully tested in the visual, somatosensory, and frontal cortex, demonstrating its capability for simultaneous electrophysiological and fluorescent measurements. These results highlight the potential of the ECoGScope platform to advance the development of multifunctional tools for studying brain function and addressing neurological disorders.

1. Introduction

The investigation of neural circuits has led to significant advancements in neuroscience, enhancing the general comprehension of brain disease mechanisms (Busche and Konnerth, 2016; Carlson et al., 2006; McGregor and Nelson, 2019; Parikshak et al., 2013; Rajasethupathy et al., 2016), diagnosis (Wandell and Le, 2017; Yasaka et al., 2021), and treatment (Canter et al., 2016; Housley et al., 2021; Vázquez-Guardado et al., 2020). Historically, studies have focused on elucidating the physical connections among distinct brain regions (Lynn and Bassett, 2019; Pessoa, 2014). However, recent attention has shifted toward the concept of functional connectivity (Chaudhuri et al., 2015; Huo et al., 2020; Kim et al., 2022; Segal et al., 2023). To better understand brain networks from this perspective, it is essential to develop multifunctional neural interfaces that can accurately record various types of neural signals. The key advancements in this field are related to improved electrophysiological signal acquisition, enabling precise real-time

monitoring of brain activity (Kuzum et al., 2014; Toda et al., 2011; Zátonyi et al., 2018; Zhang et al., 2018).

The use of real-time electrophysiological signal recording and fluorescence imaging has emerged as an effective strategy for studying the intricate connections and complex functions of the brain (Zhang et al., 2024). The high temporal resolution of electrical signals, which are correlated with neuronal activity, enables the identification of a single neuron action potentials and the accumulation of local dynamics across the neural networks (Zhang et al., 2024). Meanwhile, fluorescence imaging reveals a diverse array of neural activity by employing genetically encoded indicators, which are cell-specific, to quantify intracellular calcium (Ca²⁺) changes and distinguish between multiple cell types (Chou et al., 2022; Driscoll et al., 2021; Lu et al., 2018; Zhang et al., 2018). Therefore, the simultaneous recording of electrical signals and fluorescence imaging, with their beneficial spatial and temporal resolutions, may offer advanced insights into the brain's complex behavior. Over the last decade, electrophysiological recording devices have

a Emotion, Cognition, & Behavior Research Group, Korea Brain Research Institute 61, Cheomdan-ro, Dong-gu, Daegu, 41062, Republic of Korea

^b Department of Brain Sciences, Daegu Gyeongbuk Institute of Science and Technology (DGIST), Daegu, 42988, Republic of Korea

^{*} Corresponding author. Emotion, Cognition, & Behavior Research Group, Korea Brain Research Institute 61, Cheomdan-ro, Dong-gu, Daegu, 41062, Republic of Korea.

^{**} Corresponding author. Department of Brain Sciences, Daegu Gyeongbuk Institute of Science and Technology (DGIST), Daegu, 42988, Republic of Korea. E-mail addresses: jawook.koo@kbri.re.kr (J.W. Koo), nschou@kbri.re.kr (N. Chou).

[#] These authors contributed equally.

¹ Lead contact.

been integrated with optical monitoring techniques to examine calcium (Ca^{2+}) dynamics, which are crucial for studying the neural circuits involved in various neurological diseases and brain functions (Cameron et al., 2017; J. L. Chen et al., 2013; Wei et al., 2020; Zhang et al., 2018). Three techniques are commonly used to investigate the Ca^{2+} concentration in vivo: (1) fiber photometry (Chen et al., 2013; Sych et al., 2019), (2) two-photon calcium imaging (Mank et al., 2008; Stosiek et al., 2003), and (3) single-photon calcium imaging (Ghosh et al., 2011; Jacob et al., 2018; Laing et al., 2021). For example, a versatile customized fiber photometry system, combined with in vivo electrophysiological recording, has been used to elucidate field potentials and Ca^{2+} transitions, recorded in parallel (Chen et al., 2013). Also, an electrical recording system integrated with two-photon calcium imaging allows monitoring of the local field potential in multisite brain regions while identifying the activation of distinct cell types (Tort-Colet et al., 2023).

Additionally, microelectrode arrays coupled with single-photon imaging, which combine the benefits of previously proposed electrooptical recording devices, have been developed to study the functional connectivity of the brain (Erofeev et al., 2024; Housley et al., 2021; Todaro et al., 2019). While miniature microendoscopes, also known as single-photon imaging devices, offer lower resolution compared to two-photon imaging systems, they are widely adopted in neuroscience research due to several key advantages. These include their compact size, lightweight design, and cost-effectiveness, making them particularly suitable for studies involving freely moving animals (Glas et al., 2019; Guo et al., 2023; Laing et al., 2021; Lu et al., 2018; Ohayon et al., 2018). Specifically, their relatively low weight minimizes physical constraints on small animals, enabling naturalistic experiments without compromising mobility (Ghosh et al., 2011; Jacob et al., 2018). Moreover, these devices provide a wider field of view compared to two-photon and fiber photometry systems, allowing researchers to observe broader neural activity (Glas et al., 2019; Guo et al., 2023). Finally, their straightforward design reduces setup time and costs, making them accessible and practical for a variety of experimental applications (Jacob et al., 2018).

Herein, we present a multimodal system (i.e., ECoGScope) which integrates: 1) an ECoG electrode array for recording neural signals, 2) a microendoscope for the measurement of fluorescent signals, and 3) a custom-designed connection module for seamless integration between the ECoG electrode array and the microendoscope. To simultaneously record the fluorescent and electrophysiological signals on the cortex, the ECoG electrode array is integrated into the recording site of the microendoscope, using a mesh design for the electrode's pad and trace. We also designed the custom connection module to minimize behavioral restrictions on animals during testing. Additionally, we developed an insertion protocol to ensure precise and stable implantation of the system, which enabled stable signal recording and imaging for at least 1 week without significant signal degradation Finally, we validated the performance of this multifunctional neural interface in multiple brain regions, including the visual, sensory, and frontal cortex, with appropriate stimulation.

2. Materials and methods

2.1. Fabrication and packaging process of electrocorticography (ECoG) electrode array

We fabricated parylene C-filled polydimethylsiloxane (PDMS) based ECoG electrode array using the developed fabrication procedure in the previous study (Fig. S1) (Chou et al., 2013b, 2021). Firstly, we coated a bare silicon wafer with a 5 w/v% polyacrylic acid (PAA) solution. Note that the PAA layer acted as a sacrificial layer, enabling the polymeric device to be released in water. Then, we prepared liquid PDMS (Sylgard 184 A & B, Dow Corning, USA) with 10:1 mixing ratio and spin-coated on the wafer at a thickness of 150 μ m. After that, we deposited the first parylene-C layer with a thickness of 1 μ m, using chemical vapor

deposition (NRPC-500, Nuri-Tech Corp., Incheon, Korea) on a PDMS substrate. To make the PPX layer, O_2 reactive ion etching (VITA 8, FEMTO SCIENCE, Hwaseong-si, Korea) was performed at a power of 100 W for 5 min to remove the first parylene layer from the top surface of the PDMS. Next, using e-beam evaporation (EL-5, ULVAC, Methuen, MA, USA), titanium (Ti) and gold (Au) layers were deposited at 20 nm and 200 nm thicknesses on the PPX layer, respectively. At this process, the metal layer was patterned by inductive coupling plasma (Plasma Lab100, Oxford Instruments, Abingdon, England) etching to form electrodes and signal lines. After that, the second parylene-C layer with 5 μ m for insulation was deposited on the top substrate, and it was patterned by O_2 reactive RIE process to open electrodes and contact pads. Finally, we removed the remaining photoresist and released the electrode in deionized (DI) water to detach from the wafer.

The developed ECoG electrode array was packaged according to the following procedure. First, the electrode array was connected to a custom printed circuit board (PCB) using conductive thermal epoxy (Duralco 125, Cotronics, Brooklyn, NY, USA). Following this, electrode integrated on PCB was stored at 90 °C for 2 h to provide mechanical and electrical stability. Lastly, the Omnetics connector (A79038-001, Omnetics, Minneapolis, MN, USA) was soldered on the other side of the PCB to provide electrical connections between the ECoG electrode array and the Intan recording system.

2.2. Fabrication of miniaturized connection module

We have designed a miniaturized connection module system that was manufactured using the Ultimaker 2^+ 3D printer (Ultimaker BV, Geldermalsen, Netherlands). The connection module comprised three components, i.e., base plate, supporter, and protector. The primary role of each part was as follows. First, the base plate combined the electrode array and the microendoscope, and the supporter held the electrode array on the mouse's head. Lastly, the protector played a role in protecting the developed electrode array from the external environment. The connection module's size was approximately 6 x 6 \times 10 mm (WDL, Width x Depth x Length), and it weighs 0.48 g.

2.3. In vivo recording and signal analysis

ECoG signals were recorded using the Intan recording system (Intan RHD 512 system, Intan technologies, Los Angeles, CA, USA). The raw signals were filtered and digitized through the Intan software at a 20 ${\rm ks}^{-1}$ sampling rate per channel. Also, a 1 Hz to 1 kHz band-pass filter and a 60 Hz notch filter was applied to the recorded signals.

The electrophysiological signals were analyzed using various analysis tools provided by Origin. Specifically, a short-time Fourier transform (STFT) was applied to extract spectral power features from local field potentials (LFPs). Additionally, Fast Fourier Transform (FFT) analysis was employed to calculate parameters such as magnitude, amplitude, and power spectra expressed as mean square amplitude (MSA). An FFT filter was further applied to isolate signals corresponding to specific brain wave frequencies. We evaluated the frequency components of the recorded signal from each electrode and applied a bandpass filter that adopted appropriate filters corresponding to theta (4-8 Hz), alpha (8-13 Hz), beta (13-30 Hz), low-gamma (30-60 Hz), and high-gamma (60-100 Hz) waves. The power spectra were calculated as follows: First, a band-pass filter was applied to the raw LFP signals for each frequency band. Next, FFT was performed to compute the power spectra expressed as MSA. The power for each frequency band was then obtained by averaging the MSA values within the corresponding frequency range. For instance, theta power was calculated by averaging the MSA values between 4 Hz and 8 Hz. This process was repeated for the theta, alpha, beta, low-gamma, and high-gamma bands, with calculations performed separately for each electrode.

The fluorescence signal representing neuronal activity was obtained by open-source software of the UCLA V4 Miniscope (Miniscope DAQ software 1.0, GitHub version August 30, 2020), at 10 frames per second. Note that we injected AAV-PHP.eB-syn-jGCaMP7f for in vivo recording. The acquired fluorescence images were then imported into ImageJ, where contrast adjustments were applied to reduce background noise. Intensity profile data over time were extracted and further quantified as $\Delta F/F_0$, calculated using the formula $\Delta F/F_0 = (F-F_0)/F_0$. Here, F represents the fluorescence intensity at a given time point, and F_0 is the baseline fluorescence intensity, determined immediately after the start of signal acquisition.

2.4. Data and statistical analysis

We conducted all statistical analyses using GraphPad Prism 9 (GraphPad Software) and Origin Pro 2024 (OriginLab). The key metrics used include: p-value: represents the probability that the observed results occurred by chance, with values below 0.05 considered statistically significant. F-value: derived from ANOVA, it compares variance between groups to variance within groups. A larger F-value suggests greater group differences, and when paired with a small p-value,

indicates statistical significance. n: refers to the sample size, typically the number of observations or animals included in each experimental group. Normality was assessed using the Shapiro–Wilk test, and equality of variances was assessed using Bartlett's test (or F-test). The details of specific statistical tests and their outcomes are provided in the related figure legends. Illustrations (Figs. 3A, 4A and 5A) were created with BioRender.com.

3. Results and discussion

3.1. Development of the ECoGScope platform

We developed the ECoGScope platform to integrate a microendoscope and ECoG electrode array for the simultaneous recording of fluorescence and electrophysiological signals on the cortex, without restricting the behavior of mice (Fig. 1A and B). This platform consisted of an ECoG electrode array for recording electrophysiological signals, a commercial microendoscope (UCLA miniscope V4, LABmaker, Berlin, Germany) for fluorescence imaging, and a custom-designed connection

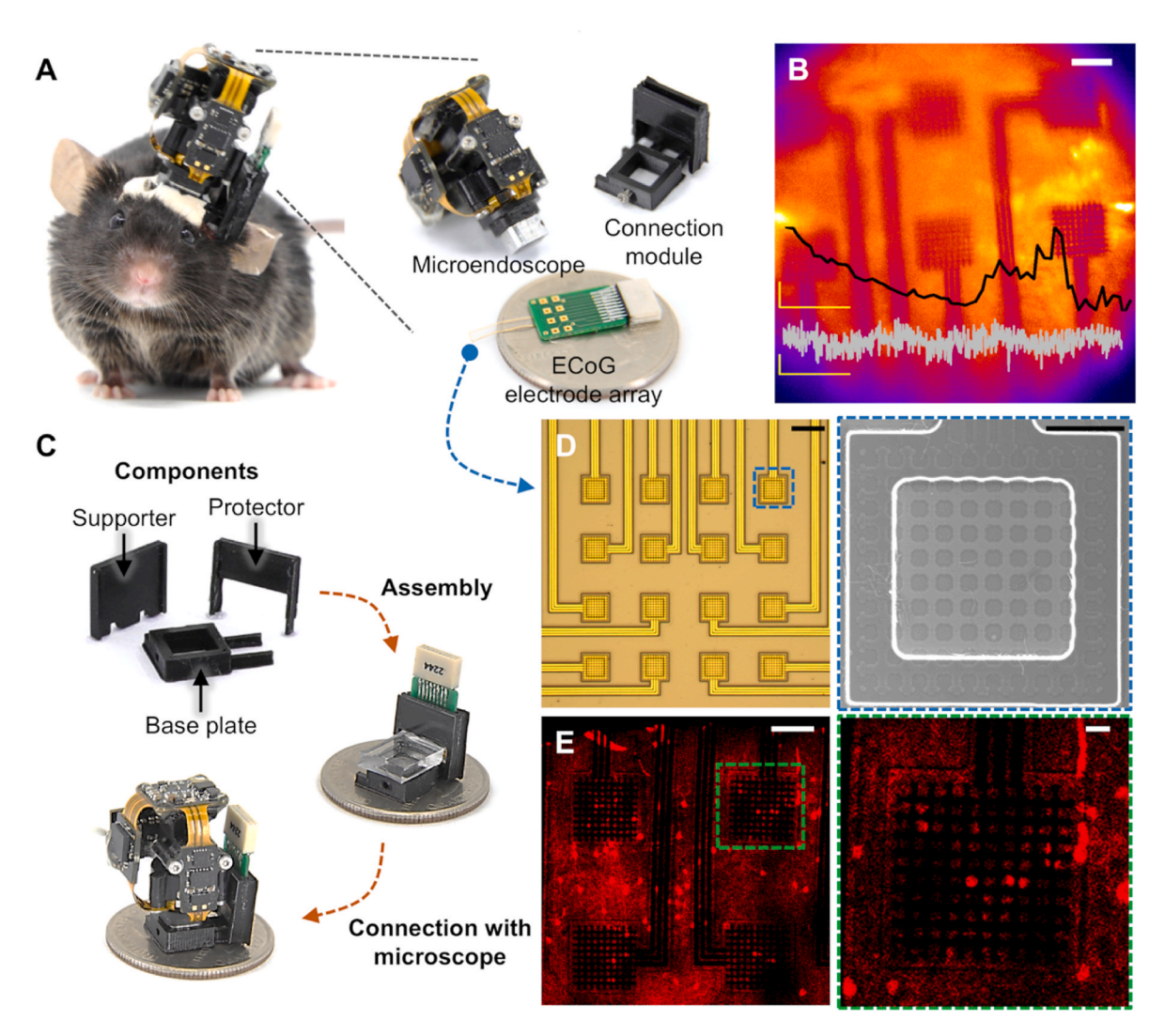


Fig. 1. Design and features of the ECoGScope platform.

- (A) Photographs of a mouse with the ECoGScope platform mounted on its head and the overall system configuration used for the parallel recording of neural signals and fluorescence images.
- (B) Simultaneous recording of electrophysiological and fluorescence signals using the ECoGScope platform. Scale bar: 100 μ m. ECoG signal scale bar: 400 μ V (vertical) and 0.2 s (horizontal). Fluorescence signal scale bar: 4% (vertical) and 0.2 s (horizontal).
- (C) Assembled photographs displaying the microendoscope and ECoG electrode array connected via a customized connection module.
- (D) Optical and SEM images of the ECoG electrode array. Scale bar: 200 µm (left) and 50 µm (right).
- (E) Multiple cells observed by fluorescence microscopy using the ECoG microelectrode array. Scale bar: 100 µm (left) and 20 µm (right).

module that integrated the ECoG electrode array with the microendoscope (Fig. 1A). The connection module, fabricated using a 3D printer, was comprised of three components: a base plate, a supporter, and a protector. The specific assembly procedures are outlined as follows (Fig. 1C). First, the ECoG electrode array was attached to the front of the supporter. The electrode-attached supporter was then securely fixed to the base plate using adhesive. Finally, a protective covering was glued to the outer part of the supporter to shield the ECoG electrode array from external forces. The ECoG electrode array weighed 0.20 g, the connection module weighed 0.48 g, and the microendoscope weighed 3.0 g, resulting in a total device weight of 3.68 g. Given that the

weight of the ECoGScope integrated with a commercial module stood at 3.57 g, our system demonstrated a negligible weight difference from the configuration mentioned above. This suggests that the developed system maintains a weight profile that does not inflict undue strain on the subject animal.

The ECoG electrode array was fabricated using polydimethylsiloxane (PDMS), a material widely recognized for its biocompatibility, transparency, and high flexibility (Fig. 1D)(Chou et al., 2013b; Lee et al., 2020). PDMS played a pivotal role in this platform, particularly due to its suitability for neural interfacing and its ability to conform closely to biological tissues. Notably, its mechanical properties, with a Young's

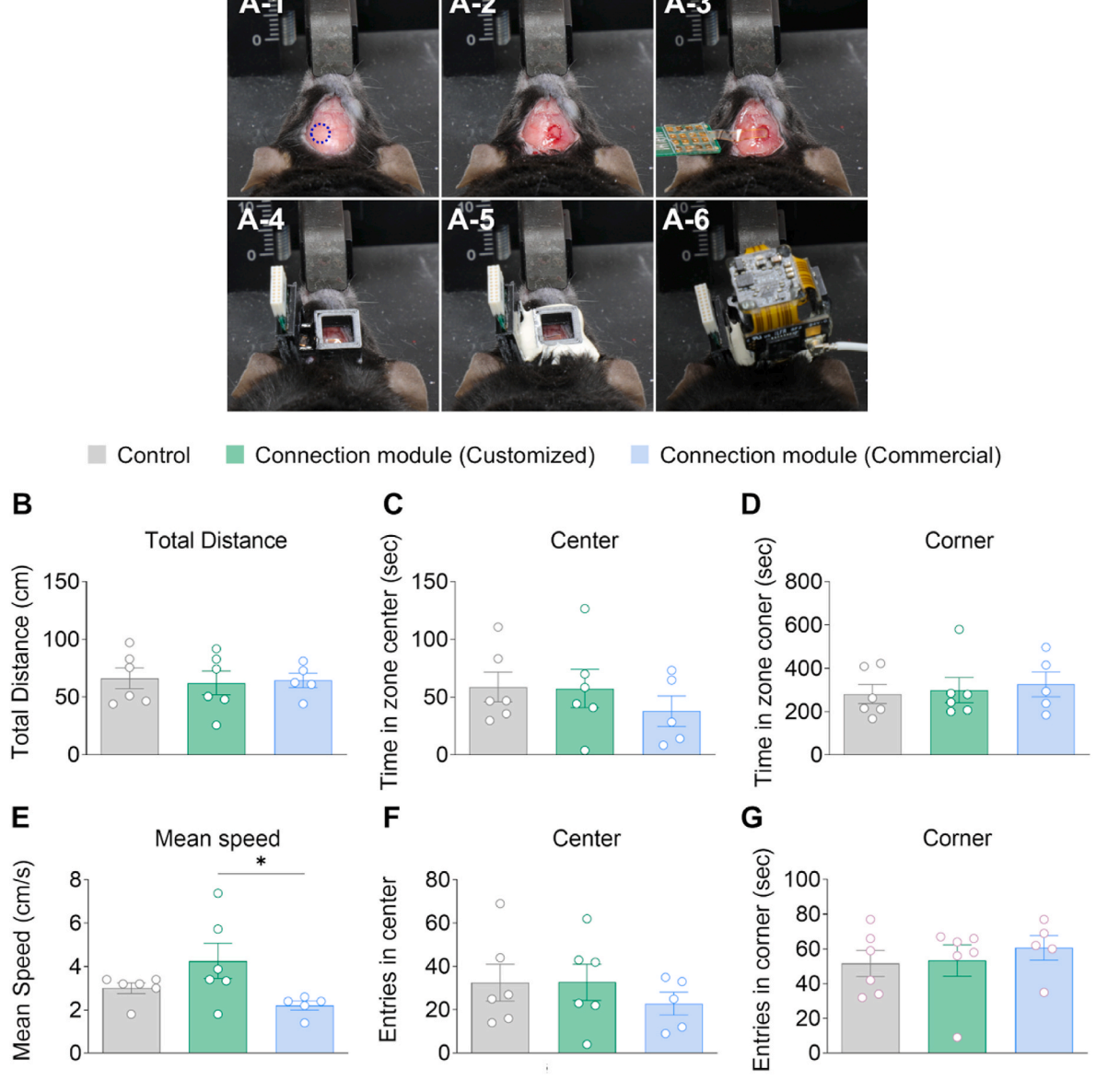


Fig. 2. Surgery protocol and behavior validation.

(A1-A6) Surgical procedures used for assembling the ECoGScope platform on a mouse's head.

- (B) Overall traveled distance (One-way ANOVA with Tukey's multiple comparisons post-hoc test, $F_{2,\ 14}=0.5558,\ p=0.9460,\ n=6,\ 6,\ 5$).
- (C) Time spent in the center for each group (One-way ANOVA with Tukey's multiple comparisons post-hoc test, $F_{2,\ 14}=0.6124,\ p=0.5560,\ n=6,\ 6,\ 5).$
- (D) Time spent in the corners for each group (One-way ANOVA with Tukey's multiple comparisons post-hoc test, $F_{2, 14} = 0.1665$, p = 0.8483, n = 6, 6, 5).
- (E) Mean movement speed within each group chamber (One-way ANOVA with Dunn's multiple comparisons post-hoc test, H = 6.614, p = 0.0289, n = 6, 6, 5).
- (F) Number of entries into the center (One-way ANOVA with Tukey's multiple comparisons post-hoc test, F2, 14 = 0.4914, p = 0.6220, n = 6, 6, 5).
- (G) Number of entries into the corners (One-way ANOVA with Tukey's multiple comparisons post-hoc test, F2, 14 = 0.3263, p = 0.7269, n = 6, 6, 5).

All statistical analyses were preceded by normality tests and tests for homogeneity of variance to ensure that appropriate hypothesis tests were applied. Statistical significance was defined as follows: *p < 0.05, **p < 0.01, ***p < 0.001, ****p < 0.0001, while p > 0.05 indicates no statistical significance. Bar graphs represent mean \pm SEM.

modulus close to 1 MPa, closely resemble those of biological tissues, making it an ideal choice for neural interfacing applications (Lee et al., 2020; Moon et al., 2024a, 2024b). The fabrication process using PDMS was developed based on a previous report, and the details provided in the experimental procedure section and the supplementary information (Fig. S1)(Chou et al., 2013a). To ensure conformal contact between the electrode and the brain surface, we selected PDMS with a thickness of approximately 100 μm or less as the main material for the electrode (Moon et al., 2024b). We designed the electrode recording site with a mesh structure to detect activated cells while simultaneously recording

ECoG signals optically. Each recording site was 500 $\mu m \times 500~\mu m$, with 16 recording sites arranged in a 4 \times 4 matrix. To match the opening dimensions inside the mesh electrode to the size of individual cells, we measured the diameter of cells (n = 30) in the cerebral cortex, which averaged 12.5 \pm 4.1 μm . Consequently, the dimensions of the openings within the mesh electrode were set to 10 $\mu m \times$ 10 μm . Scanning electron microscopy (SEM) images provided a detailed view of the recording site (Fig. 1D).

The comprehensive features and electrochemical characterization of the fabricated ECoG electrode array are presented in the supplementary

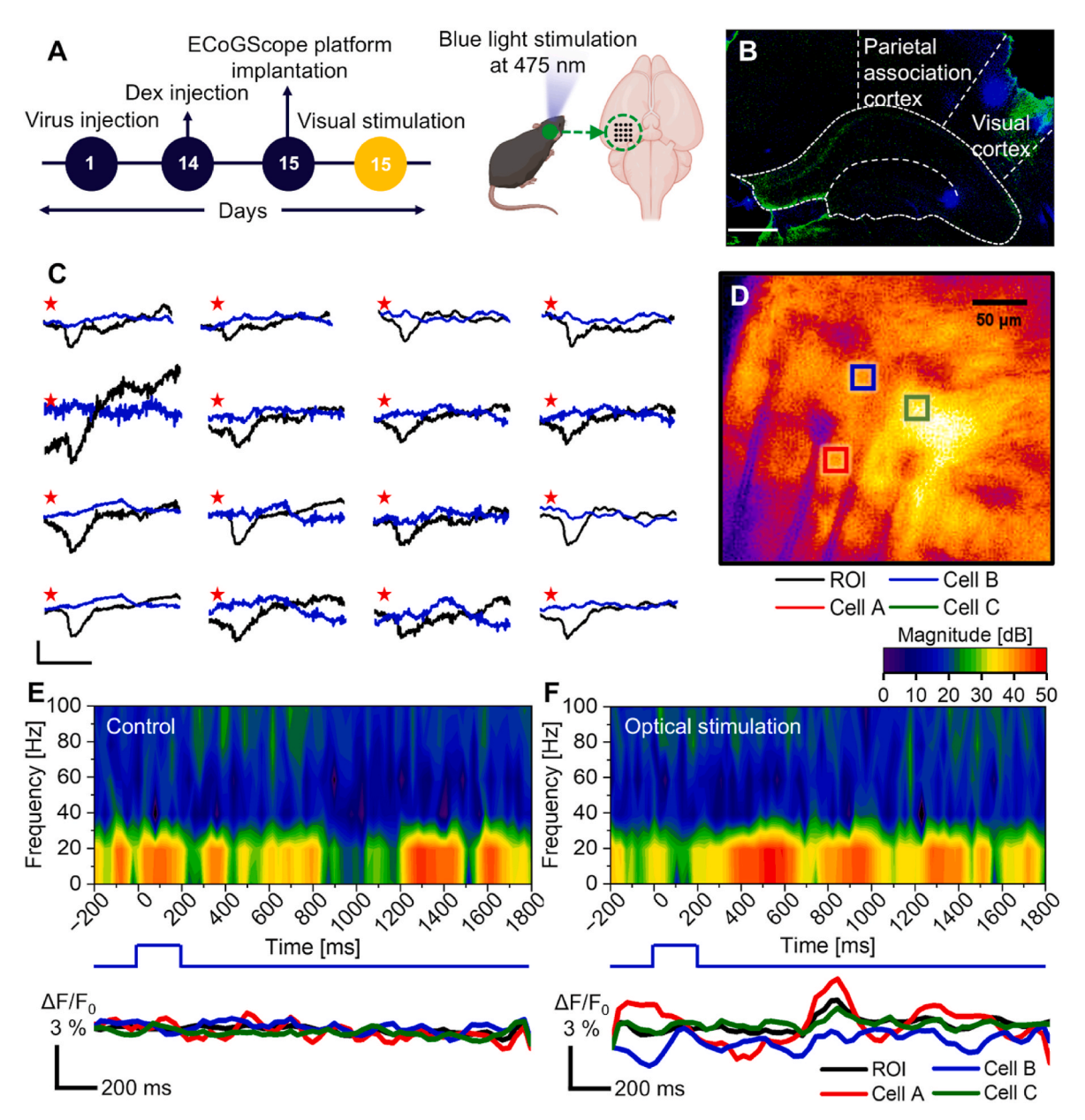


Fig. 3. Simultaneous electrical signal and fluorescence image recording from the visual cortex region.

- (A) Experimental scheme of a multimodal neural electrode array developed on the surface of the visual cortex.
- (B) Representative image of virus injection in the visual cortex. Scale bar: 500 μm.
- (C) Example of the recorded ECoG signals from 16 channels in response to light stimulation (scale bar: $500 \mu V$, vertical; 200 ms, horizontal). The data were ideal low-pass filtered at a cut-off frequency of 300 Hz. Each asterisk indicates the stimulation time. Each blue and black solid lines represent the local field potentials based on control and optical stimulation signals, respectively.
- (D) Miniscope images of the visual cortex region beneath the recording site, taken during the stimulation event. Individual activated neurons are marked by colored squares.
- (E and F) (Top) Time-frequency spectral analysis of the ECoG signal during stimulation (Bottom). $\Delta F/F_0$ traces for the entire brain region under the recording site (designated as the region of interest, ROI) and for several individual cells during the stimulation event. (For interpretation of the references to color in this figure legend, the reader is referred to the Web version of this article.)

information (Fig. S2). When comparing the electrochemical impedance spectroscopy characteristics of the non-meshed and meshed ECoG electrode arrays, the non-meshed electrode array showed an impedance of $281\pm70~\Omega$ with a phase of approximately -65° (n = 8) at 1 kHz, while the meshed electrode exhibited an impedance of $358\pm20~\Omega$ with a phase of approximately -60° (n = 8). The minimal differences in impedance and phase between the two electrode types suggest that the meshed ECoG electrode array is compatible with the standard ECoG electrode array. Additionally, the transparency of the PDMS layer and the size match between the recording site openings and the cells enabled to clearly distinguish individual cells beneath the electrode during in vitro and in vivo studies (Fig. 1E).

3.2. Implantation of ECoGScope and behavioral monitoring

As mentioned above, the ECoGScope device was designed to enable simultaneous electrophysiological and fluorescence measurements with minimal impact on animal behavior. Its design integrates a meshstructured electrode array, a custom connection module, and an integrated microendoscope, ensuring stable performance during in vivo experiments.

To implement this system, we optimized a surgical procedure for the mouse brain, seamlessly integrating the implantation process with the device's functionality (Fig. 2A). The surgical steps were as follows: First, a hole matching the electrode dimensions was created in the target cortical region to ensure precise electrode placement (Figs. 2A–1 and 2A-2). Next, the ECoG electrode array was positioned on the cortex and secured using the customized connection module to achieve stable electrical recordings (Figs. 2A–3 and 2A-4). Dental cement was then applied around the assembly to enhance stability and minimize movement artifacts (Figs. 2A–5). Once the dental cement hardened, the microendoscope was installed, and a ground wire was implanted inside the skull to complete the setup (Figs. 2A–6).

To assess the behavioral influence of the implant, we conducted an open field test (OFT) to compare the behavior between mice equipped with a commercially available base plate from UCLA to those fitted with

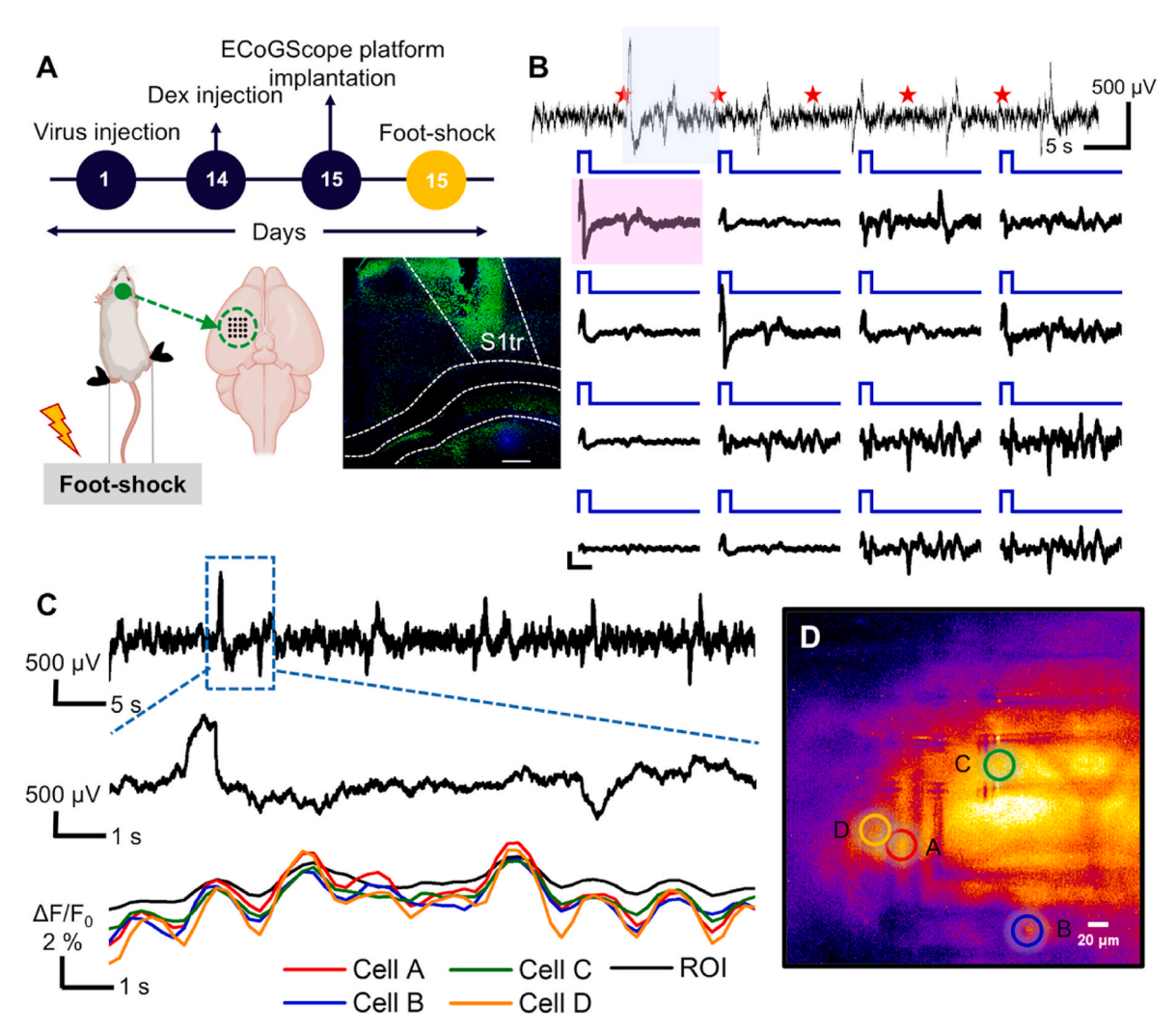


Fig. 4. Simultaneous electrical signal and fluorescence image recording from the somatosensory region.

(A) (Top) Experimental scheme of displaying the experimental setup. (Bottom) Placement of the developed multimode neural electrode array on the surface of the sensory cortex, along with fluorescence images from fixed brain slices of GCaMP7f-expressing mice. Scale bar: 200 µm.

(B) Recorded ECoG signals from 16 channels in response to foot shock (scale bar: 1 mV, vertical; 2 s, horizontal). The data were ideal low-pass filtered at a cut-off frequency of 300 Hz.

(C) (Top) ECoG signal in response to electrical shock. (Middle) Magnified ECoG signal during the stimulated state. (Bottom) Fluorescence intensity ($\Delta F/F_0$) corresponding to the ECoG signal.

(D) Calcium images taken from the sensory cortex region beneath the recording site during the stimulation event. Individual activated neurons are marked by colored circles.

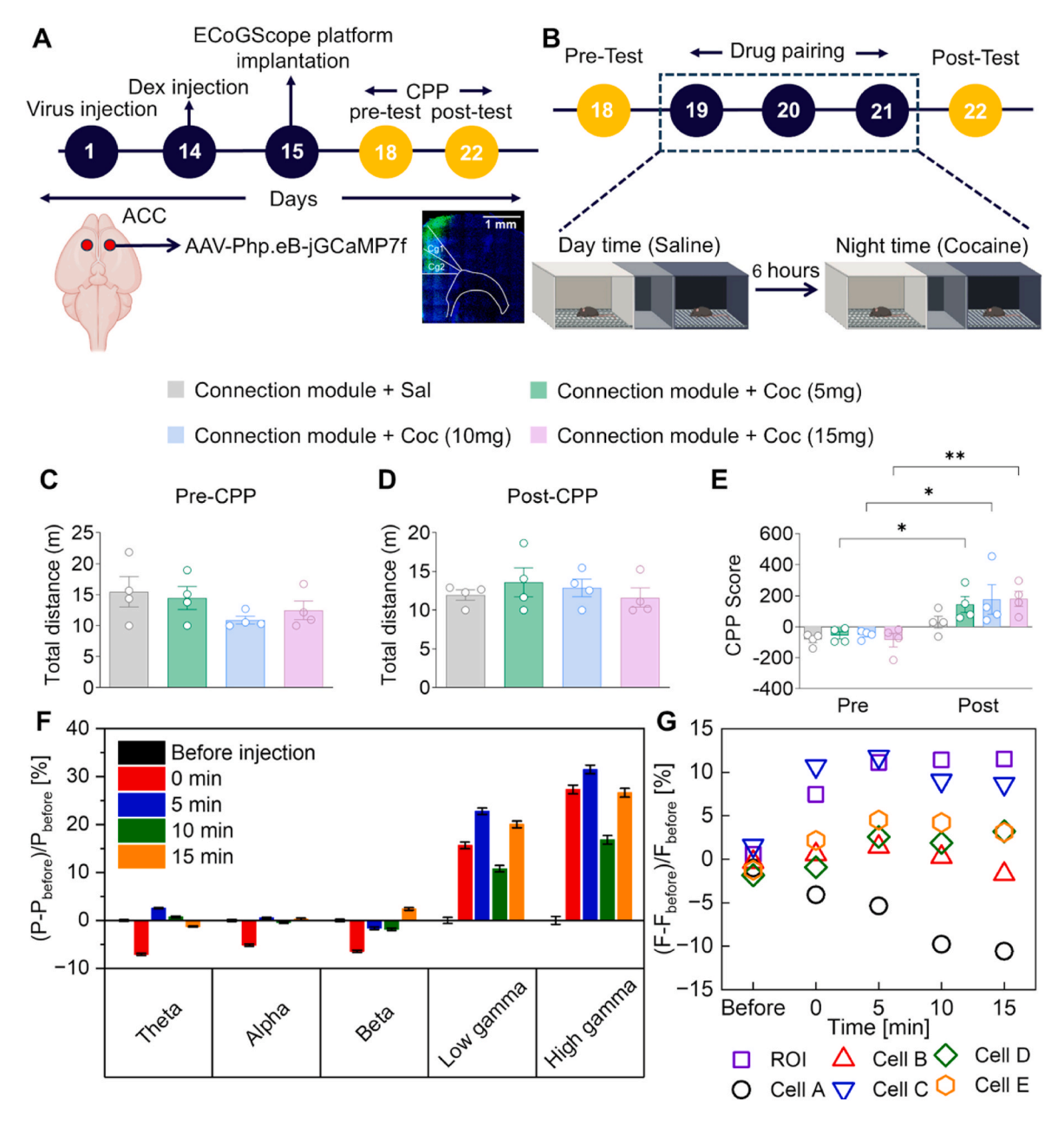


Fig. 5. Impacts of chronic cocaine exposure on ECoG signals and ACC gamma activity.

(A and B) Schematic diagram of in vivo recording using cocaine behavior test.

(C and D) Total distance traveled by each group before (One-way ANOVA with Tukey's multiple comparisons post-hoc test, $F_{3, 12} = 1.393$, p = 0.2927, n = 4) and after cocaine injection (One-way ANOVA with Tukey's multiple comparisons post-hoc test, $F_{3, 12} = 0.4638$, p = 0.7128, n = 4).

- (E) Preference for drug-paring chamber by group (Two-way ANOVA with Bonferroni's multiple comparisons post-hoc test, Interaction: $F_{3, 12} = 0.9263$, p = 0.4431; Row Factor: $F_{1, 24} = 35$, p < 0.0001; Column Factor: $F_{3, 22} = 1.358$, p = 0.2794).
- (F) Power spectral analysis of recorded ECoG signals in the theta, alpha, beta, low-gamma, and high-gamma frequency bands. Each bar chart shows the average value of 6 different electrodes, and the error bar represents the standard deviation.
- (G) Averaged Ca²⁺ fluorescence intensity change (dF/F, normalized to initial intensity) in the ROI and individual cells before and after cocaine injection.

 All statistical analyses were preceded by normality tests and tests for homogeneity of variance to ensure that appropriate hypothesis tests were applied. Statistical

All statistical analyses were preceded by normality tests and tests for homogeneity of variance to ensure that appropriate hypothesis tests were applied. Statistical significance was defined as follows: *p < 0.05, **p < 0.01, ***p < 0.001, ****p < 0.0001, while p > 0.05 indicates no statistical significance. Bar graphs represent mean \pm SEM.

our custom base plate. Both base plates were essential components of the microendoscope system, designed to securely mount the microendoscope onto the animal's head. Detailed designs of each base plate were provided in the supplementary information (Fig. S3). Following a 10-min OFT, we confirmed that mice fitted with the customized base plate exhibited the same level of locomotor function as those with the commercial base plate (Fig. S3).

We further examined whether the base plate induced any motor

deficits by comparing mice fitted with the base plate to a control group. The control group consisted of mice whose skulls were surgically opened and then sutured without any base plate attachment. We compared this group with two others: one fitted with the commercial base plate and another fitted with our custom base plate. Then, we conducted the OFT while the mice were equipped with a microendoscope to detect any potential abnormalities between the groups.

No significant differences were observed in the total distance

traveled between control mice without any equipment and those wearing the ECoGScope platform (Fig. 2B). Additionally, all mice displayed comparable times spent in the center and corners of the chamber (Fig. 2C and D), indicating that wearing the ECoGScope platform did not induce anxiety.

Moreover, when analyzing average speed to assess potential impacts on movement, we found that the group equipped with the custom connection module exhibited slightly higher speeds than the group equipped with the commercial connection module (Fig. 2E). However, the entrance rates to the center and corners were comparable among the control mice and those fitted with either the custom or commercial modules (Fig. 2F and G). These findings suggest that our developed connection module does not influence baseline anxiety or motor function in mice.

3.3. In vivo multimodal recording in the acute stage

To demonstrate the functionality of the ECoGScope, we recorded visual evoked potentials (VEPs) from the primary visual cortex of anesthetized mice. Neurons in this region were known for their sensitivity to directional visual stimuli, typically within the visible wavelength range. We injected AAV-PHP.eB-syn-jGCaMP7f, a genetically encoded calcium indicator (GECI) driven by the synapsin (syn) promoter, enabling neuron-specific expression (Kügler et al., 2003). This GECI combines a circularly permuted enhanced green fluorescent protein (EGFP) with calmodulin (CaM) and a CaM-binding peptide (M13). Upon calcium binding, interactions between CaM and M13 induce conformational changes in EGFP, increasing fluorescence intensity (Grienberger and Konnerth, 2012; Luo et al., 2018). Two weeks post-injection, the ECoGScope was applied to the cortical surface, and a microendoscope was attached for real-time visualization of calcium dynamics (Fig. 3B).

To simultaneously record VEPs and neuronal responses to visual stimuli, we delivered 475 nm wavelength (blue) light to the eyes of anesthetized, head-fixed mice (Fig. 3A). An LED array was placed in front of the right eye, flickering for 200 ms every 2 s to induce visual stimulation. As expected, VEPs were detected across all 16 individual electrodes of the ECoG array attached to the visual cortex during light stimulation (Fig. 3C).

To control for optical and electrical artifacts, we conducted experiments where mice were exposed to blue light stimulation, but their view was obstructed, preventing them from seeing the light. Considering the ECoG signals obtained under these conditions, we found significant differences in VEPs compared with those observed under unobstructed conditions (Fig. 3C). Specifically, VEPs recorded with direct LED exposure showed clear positive and negative peaks, consistent with previous (Glas et al., 2019; Osanai et al., 2010) studies (Jeong et al., 2021; Lee et al., 2020). In contrast, when the mice were unable to see the light despite the stimulus, the VEPs resembled a baseline state.

Furthermore, we aimed to record ECoG signals and cellular responses associated with changes in calcium (Ca^{2+}) concentration, in parallel with visual stimulation. Notably, upon exposure to the light, we observed an increase in both the electrical signals and cellular expression, including a change in the Ca^{2+} intensity within approximately 600 ms (Fig. 3E -F). This observation was consistent with several previous findings, which reported that blue light stimulation induces an increase in Ca^{2+} signals in the visual cortex within 200 ms to a maximum of 1 s (Kuznetsova et al., 2021; Osanai et al., 2010). Therefore, the developed neural interface system is capable of recording and identifying cells that are responsive to electrical signals while also revealing functional neural connectivity in specific areas of the brain.

To demonstrate the performance of the ECoGScope in other cortical areas, specifically the somatosensory cortex adjacent to the primary visual cortex, we examined whether a response could be elicited when administering a foot shock to the sensory cortex by measuring somatosensory evoked potentials (SEPs). As previously described, we injected

the AAV-PHP.eB-syn-jGCaMP7f virus into the primary somatosensory area of the trunk (S1Tr) and performed ECoG and microendoscope surgery two weeks later (Fig. 4A). After surgery, the foot of the anesthetized mice was exposed to electrical stimulation using a square wave pattern at 300 mV for 1 s, followed by a 10-s rest period, which was repeated for a total duration of 1 min. The ECoG electrode array and microendoscope were used to measure signals from the S1Tr during electrical stimulation. We confirmed that the shape and values of SEPs recorded in the S1Tr through the ECoG electrode array were closely similar to those reported in previous studies, which presented a peak latency of approximately 200 ms (Fig. 4B) (Kaiju et al., 2017a; Lu et al., 2022; Park et al., 2016).

Overall, when an electrical stimulus was applied to mice, SEPs were generated and recorded using the ECoG electrode array. Within a few seconds, an increase in the ${\rm Ca}^{2+}$ concentration was observed in the cells beneath the meshed electrodes through the microendoscope (Fig. 4C and D) (J. L. Chen et al., 2013; Chen et al., 2021; Chisholm et al., 2018; Kaiju et al., 2017b; Lu et al., 2022). These findings were consistent with previously published results, further validating the functionality and effectiveness of our system.

3.4. In vivo sustained demonstration using cocaine-addicted mice

We conducted an in vivo experiment to simultaneously record electrophysiological and fluorescence signals in the prefrontal cortex while monitoring the behaviors of cocaine-addicted mice. Previous research suggested that individuals with drug addiction often exhibited hypoactivity in the anterior cingulate cortex (ACC) when processing information compared to those without addiction issues (Designed Research et al., 2009). Therefore, we aimed to determine whether cocaine addiction leads to decreased activity in the ACC using the ECoGScope.

For this experiment, we injected AAV-PHP.eB-syn-jGCaMP7f into the ACC and implanted the ECoG electrode array two weeks later (Fig. 5A). To assess cocaine addiction, we conducted a conditioned place preference (CPP) test (Fig. 5B and C, and S4). Given the one-week duration of the experiment, we administered dexamethasone intraperitoneally to alleviate potential inflammatory reactions. Initially, we conducted an experiment to determine the optimal dosage of cocaine for effective action in the ACC. Subjects were divided into three groups, receiving doses of 5, 10, or 15 mg/kg, while the control group received saline injections (Fig. S5). Prior to drug administration, a pre-CPP test was conducted to assess locomotor function and individual chamber preference. No significant differences were observed in locomotor function among the groups, and no biased chamber preference was detected (Fig. 5C, D, 5E, S4, and S5).

Building on the pre-CPP findings, each subject received saline in the morning and cocaine in the afternoon for three consecutive days, followed by a post-CPP test conducted 18 h after the final cocaine injection. Although there were no significant differences in total locomotor activity among the groups (Fig. 5C, D, 5E, S4, and S5), individuals administered cocaine typically showed a preference for the chamber associated with cocaine compared to those observed before CPP measurements (Figs. S4 and S5). Moreover, the 15 mg/kg dosage demonstrated a significant increase in chamber preference.

Additionally, we investigated whether 15 mg/kg of cocaine induces locomotor sensitization, a well-documented phenomenon, and confirmed that the expected effects of cocaine were observed (Figs. S4E and S4F). Based on these findings, we proceeded with experiments utilizing the 15 mg/kg dosage owing to its enhanced effectiveness.

We specifically analyzed ECoG signals across different frequency bands, namely theta (4–8 Hz), alpha (8–13 Hz), beta (13–30 Hz), low gamma (30–60 Hz), and high gamma (60–100 Hz), to observe the changes in power ratios in response to cocaine administration (Fig. 5F). The power levels in the theta, alpha, and beta ranges showed no significant fluctuations before and after cocaine administration. Notably, we observed substantial shifts in electrical activity within the gamma

band. At the 10-min mark after cocaine administration, both the low and high gamma power increased (Fig. 5F). These findings are consistent with previous studies that reported an increase in low and high gamma power across multiple brain regions, including the prefrontal cortex and orbitofrontal cortex, following cocaine exposure in rodents (McCracken and Grace, 2013). Moreover, the instability and reduction in low and high gamma power have been associated with cognitive impairments, suggesting a potential mechanism through which cocaine affects cognitive function (Booth et al., 2016; Mably et al., 2017). By replicating patterns observed in prior research, our findings demonstrate the robustness and reliability of our system in capturing neural dynamics.

Note that the gamma oscillations, which decreased at the 10-min mark, subsequently increased (Fig. 5F). This transient reduction followed by an increase in gamma activity may be linked to the effects of cocaine on dopamine signaling (Dilgen et al., 2013). Cocaine inhibits dopamine reuptake, leading to elevated dopamine levels in the brain, which in turn affects neural oscillations, particularly within the gamma frequency range (Dilgen et al., 2013).

To further investigate these changes at the cellular level, we employed fluorescence imaging in parallel with ECoG recordings (Fig. 5G and S6). The fluorescence signals provided a dynamic view of neuronal activity, particularly in the ACC, a region implicated in cognitive processing and addiction (Designed Research et al., 2009). Our results showed that the fluorescence intensity fluctuated in close correspondence with the electrophysiological signals, exhibiting approximately a 10% variation in relation to the observed changes in gamma activity (Fig. 5G). This real-time visualization confirmed that the neural alterations detected using the ECoG electrode array were reflected in the fluorescence data, offering a complementary perspective on the effects of cocaine at the neuronal level.

Cocaine-induced dopaminergic hyperactivity results from dopamine transporter (DAT) inhibition, increasing extracellular dopamine levels (Sulzer, 2011). This enhanced dopaminergic signaling, particularly through D1 receptors in the prefrontal cortex, triggers calcium influx via L-type voltage-gated calcium channels (VGCC), raising intracellular calcium levels (Surmeier et al., 2007). Using GCaMP7f, we observed significant changes in calcium transients in neurons, especially in the ACC, following cocaine i.p. These calcium dynamics serve as an indirect measure of dopamine activity. Together, our findings demonstrate that cocaine induces significant and lasting alterations in gamma activity, highlighting the integrated insights into neural dynamics provided by simultaneous electrophysiological and fluorescence imaging.

4. Conclusion

In summary, we present the ECoGScope, a multifunctional neural interface platform that integrates ECoG electrode arrays with a microendoscope enabling simultaneous electrophysiological recordings and fluorescence imaging. The mesh-type PDMS-based electrode array ensures precise signal acquisition and unobstructed optical monitoring of cellular activity, while the compact connection module minimizes interference with natural animal behavior. The system was validated across various cortical regions, demonstrating its ability to record VEPs and SEPs and capture Ca²⁺ signal changes, even in complex experimental models such as cocaine addiction.

The results highlight the ECoGScope's potential to advance neuroscience research by enabling the study of functional connectivity and brain dynamics with unprecedented detail. However, limitations include the absence of integrated optical stimulation, drug delivery, and chemical sensing capabilities, which could further enhance its versatility.

Future developments should address these limitations by incorporating additional functionalities to broaden the platform's applications in studying neurological disorders and developing therapeutic interventions. Overall, the ECoGScope provides a powerful and adaptable tool for exploring the mechanisms of brain function and improving the

understanding and treatment of neurological diseases.

CRediT authorship contribution statement

Jonghee Eun: Writing – original draft, Visualization, Validation, Software, Resources, Methodology, Investigation, Formal analysis, Conceptualization. Jeongseop Kim: Writing – original draft, Validation, Software, Resources, Methodology, Formal analysis, Conceptualization. Tae-Eun Kim: Resources. Ja Wook Koo: Writing – review & editing, Supervision. Namsun Chou: Writing – review & editing, Validation, Supervision, Project administration, Funding acquisition, Data curation, Conceptualization.

Declaration of competing interest

The authors declare that they have no known competing financial interests or personal relationships that could have appeared to influence the work reported in this paper.

Acknowledgments

This work has been supported by grants of the National Research Foundation (NRF-2021R1C1C2011489 and NRF-2022M3E5E9018226) and Korea Brain Research Institute research program (grant no.: 25-BR-02-02), funded by Ministry of Science and ICT, and from RS-2024-00332645 the Ministry of Health and Welfare and Ministry of Food and Drug Safety, Republic of Korea.

Appendix A. Supplementary data

Supplementary data to this article can be found online at https://doi.org/10.1016/j,bios.2025.117196.

Data availability

Data will be made available on request.

References

Booth, C.A., Witton, J., Nowacki, J., Tsaneva-Atanasova, K., Jones, M.W., Randall, A.D., Brown, J.T., 2016. J. Neurosci. 36, 350–363. https://doi.org/10.1523/ JNEUROSCI.2151-15.2016.

Busche, M.A., Konnerth, A., 2016. Philos. Trans. R. Soc. B Biol. Sci. 371. https://doi.org/ 10.1098/rstb.2015.0429.

Cameron, M.A., Kekesi, O., Morley, J.W., Bellot-Saez, A., Kueh, S., Breen, P., van Schaik, A., Tapson, J., Buskila, Y., 2017. J. Vis. Exp. https://doi.org/10.3791/55396.

Canter, R.G., Penney, J., Tsai, L.H., 2016. Nature 539, 187–196. https://doi.org/ 10.1038/nature20412.

Carlson, P.J., Singh, J.B., Zarate, C.A., Drevets, W.C., Manji, H.K., 2006. NeuroRx 3, 22–41. https://doi.org/10.1016/j.nurx.2005.12.009.

Chaudhuri, R., Knoblauch, K., Gariel, M.A., Kennedy, H., Wang, X.J., 2015. Neuron 88, 419–431. https://doi.org/10.1016/j.neuron.2015.09.008.

Chen, J.L., Andermann, M.L., Keck, T., Xu, N.L., Ziv, Y., 2013. J. Neurosci. 33, 17631–17640. https://doi.org/10.1523/JNEUROSCI.3255-13.2013.

Chen, T.-W., Wardill, T.J., Sun, Y., Pulver, S.R., Renninger, S.L., Baohan, A., Schreiter, E. R., Kerr, R.A., Orger, M.B., Jayaraman, V., Looger, L.L., Svoboda, K., Kim, D.S., 2013. Nature 499, 295–300. https://doi.org/10.1038/nature12354.

Chen, X.J., Liu, Y.H., Xu, N.L., Sun, Y.G., 2021. J. Neurosci. 41, 10330–10340. https://doi.org/10.1523/JNEUROSCI.1445-21.2021.

Chisholm, K.I., Khovanov, N., Lopes, D.M., La Russa, F., McMahon, S.B., 2018. eNeuro 5. https://doi.org/10.1523/ENEURO.0417-17.2018.

Chou, N., Jeong, J., Kim, S., 2013a. J. Micromechanics Microengineering 23. https://doi. org/10.1088/0960-1317/23/12/125035.

Chou, N., Moon, H., Park, J., Kim, S., 2021. Prog. Org. Coatings 157, 106309. https://doi.org/10.1016/j.porgooat.2021.106309.

Chou, N., Shin, H., Kim, K., Chae, U., Jang, M., Jeong, U., Hwang, K., Yi, B., Lee, S.E., Woo, J., Cho, Y., Lee, C., Baker, B.J., Oh, S., Nam, M., Choi, N., Cho, I., 2022. Adv. Sci. 9, 2103564. https://doi.org/10.1002/advs.202103564.

Chou, N., Yoo, S., Kim, S., 2013b. IEEE Trans. Neural Syst. Rehabil. Eng. 21, 544–553. https://doi.org/10.1109/TNSRE.2012.2210560.

Designed Research; R, N.D.V.Z.G., Performed Research; R, F.T.Z.G., Pnas, D., 2009. Proc. Natl. Acad. Sci. 106.

Dilgen, J.E., Tompa, T., Saggu, S., Naselaris, T., Lavin, A., 2013. Front. Cell. Neurosci. 7, 1–9. https://doi.org/10.3389/fncel.2013.00213.

- Driscoll, N., Rosch, R.E., Murphy, B.B., Ashourvan, A., Vishnubhotla, R., Dickens, O.O., Johnson, A.T.C., Davis, K.A., Litt, B., Bassett, D.S., Takano, H., Vitale, F., 2021. Commun. Biol. 4. https://doi.org/10.1038/s42003-021-01670-9.
- Erofeev, A.I., Vinokurov, E.K., Antifeev, I.E., Vlasova, O.L., Bezprozvanny, I.B., 2024. IJ. Evol. Biochem. Physiol. 60, 1586–1606. https://doi.org/10.1134/ S0022093024040264.
- Ghosh, K.K., Burns, L.D., Cocker, E.D., Nimmerjahn, A., Ziv, Y., Gamal, A. El, Schnitzer, M.J., 2011. Nat. Methods 8, 871–878. https://doi.org/10.1038/ nmeth.1694.
- Glas, A., Hübener, M., Bonhoeffer, T., Goltstein, P.M., 2019. PLoS One 14, e0214954. https://doi.org/10.1371/journal.pone.0214954.
- Grienberger, C., Konnerth, A., 2012, 73, 862–885. https://doi.org/10.1016/j.neuron.20 12.02.011.
- Guo, C., Blair, G.J., Sehgal, M., Sangiuliano Jimka, F.N., Bellafard, A., Silva, A.J., Golshani, P., Basso, M.A., Blair, H.T., Aharoni, D., 2023. Sci. Adv. 9. https://doi.org/ 10.1105/ceiadv.adv.3018
- Housley, S.N., Nardelli, P., Rotterman, T.M., Cope, T.C., Coulter, W.H., 2021. Proc. Natl. Acad. Sci. 118. https://doi.org/10.1073/pnas.2100428118/-/DCSupplemental.
- Huo, Y., Chen, H., Guo, Z.V., 2020. Neuron 107, 1080–1094.e5. https://doi.org/ 10.1016/j.neuron.2020.06.038.
- Jacob, A.D., Ramsaran, A.I., Mocle, A.J., Tran, L.M., Yan, C., Frankland, P.W., Josselyn, S.A., 2018. Curr. Protoc. Neurosci. 84. https://doi.org/10.1002/cpns.51.
- Jeong, U.-J., Lee, J., Chou, N., Kim, K., Shin, H., Chae, U., Yu, H.-Y., Cho, I.-J., 2021. Lab Chip 21, 2383–2397. https://doi.org/10.1039/D1LC00117E.
- Kaiju, T., Doi, K., Yokota, M., Watanabe, K., Inoue, M., Ando, H., Takahashi, K., Yoshida, F., Hirata, M., Suzuki, T., 2017a. Front. Neural Circuits 11. https://doi.org/ 10.3389/fncir.2017.00020.
- Kaiju, T., Doi, K., Yokota, M., Watanabe, K., Inoue, M., Ando, H., Takahashi, K., Yoshida, F., Hirata, M., Suzuki, T., 2017b. Front. Neural Circuits 11, 1–13. https://doi.org/10.3389/fncir.2017.00020.
- Kim, J., Kang, S., Choi, T.-Y., Chang, K.-A., Koo, J.W., 2022. Biol. Psychiatry. https://doi. org/10.1016/j.biopsych.2022.01.006.
- Kügler, S., Kilic, E., Bähr, M., 2003. Gene Ther. 10, 337–347. https://doi.org/10.1038/sj.gt.3301905.
- Kuznetsova, T., Antos, K., Malinina, E., Papaioannou, S., Medini, P., 2021. J. Neurosci. Methods 362, 109287. https://doi.org/10.1016/j.jneumeth.2021.109287.
- Kuzum, D., Takano, H., Shim, E., Reed, J.C., Juul, H., Richardson, A.G., de Vries, J., Bink, H., Dichter, M.A., Lucas, T.H., Coulter, D.A., Cubukcu, E., Litt, B., 2014. Nat. Commun. 5, 5259. https://doi.org/10.1038/ncomms6259.
- Laing, B.T., Siemian, J.N., Sarsfield, S., Aponte, Y., 2021. J. Neurosci. Methods 348, 109015. https://doi.org/10.1016/j.jneumeth.2020.109015.
- Lee, K.Y., Moon, H., Kim, B., Kang, Y.N., Jang, J., Choe, H.K., Kim, S., 2020. Adv. Mater. Interfaces 7, 2001152. https://doi.org/10.1002/admi.202001152.
- Lu, J., Chen, B., Levy, M., Xu, P., Han, B.-X., Takatoh, J., Thompson, P.M., He, Z., Prevosto, V., Wang, F., 2022. Sci 8, eabn6530. https://doi.org/10.1126/sciadv. abn6530.
- Lu, J., Li, C., Singh-Alvarado, J., Zhou, Z.C., Fröhlich, F., Mooney, R., Wang, F., 2018. Cell Rep. 23, 3673–3684. https://doi.org/10.1016/j.celrep.2018.05.062.
- Luo, L., Callaway, E.M., Svoboda, K., 2018. Neuron 98, 256–281. https://doi.org/ 10.1016/j.neuron.2018.03.040.
- Lynn, C.W., Bassett, D.S., 2019. Nat. Rev. Phys. 1, 318–332. https://doi.org/10.1038/ s42254-019-0040-8.
- Mably, A.J., Gereke, B.J., Jones, D.T., Colgin, L.L., 2017. Hippocampus 27, 378–392. https://doi.org/10.1002/hipo.22697.
- Mank, M., Santos, A.F., Direnberger, S., Mrsic-Flogel, T.D., Hofer, S.B., Stein, V., Hendel, T., Reiff, D.F., Levelt, C., Borst, A., Bonhoeffer, T., Hübener, M.,

- Griesbeck, O., 2008. Nat. Methods 5, 805–811. https://doi.org/10.1038/nmeth.1243.
- McCracken, C.B., Grace, A.A., 2013. J. Neurosci. 33, 17469–17482. https://doi.org/ 10.1523/JNEUROSCI.1440-13.2013.
- McGregor, M.M., Nelson, A.B., 2019. Neuron 101, 1042–1056. https://doi.org/10.1016/j.neuron.2019.03.004.
- Moon, H., Jang, J.W., Park, S., Kim, J.H., Kim, J.S., Kim, S., 2024a. Sensors Actuators B Chem 401. https://doi.org/10.1016/j.snb.2023.135099.
- Moon, H., Kwon, J., Eun, J., Chung, C.K., Kim, J.S., Chou, N., Kim, S., 2024b. Adv. Mater. Technol. https://doi.org/10.1002/admt.202301692.
- Ohayon, S., Caravaca-Aguirre, A., Piestun, R., DiCarlo, J.J., 2018. Biomed. Opt Express 9, 1492. https://doi.org/10.1364/BOE.9.001492.
- Osanai, M., Tanaka, S., Takeno, Y., Takimoto, S., Yagi, T., 2010. PLoS One 5, e13738. https://doi.org/10.1371/journal.pone.0013738.
- Parikshak, N.N., Luo, R., Zhang, A., Won, H., Lowe, J.K., Chandran, V., Horvath, S., Geschwind, D.H., 2013. Cell 155, 1008. https://doi.org/10.1016/j.cell.2013.10.031.
- Park, A.H., Lee, S.H., Lee, C., Kim, J., Lee, H.E., Paik, S.B., Lee, K.J., Kim, D., 2016. ACS Nano 10, 2791–2802. https://doi.org/10.1021/acsnano.5b07889.
- Pessoa, L., 2014. Phys. Life Rev. 11, 400–435. https://doi.org/10.1016/j.plrev.2014.03.005.
- Rajasethupathy, P., Ferenczi, E., Deisseroth, K., 2016. Cell. https://doi.org/10.1016/j.cell.2016.03.047.
- Segal, A., Parkes, L., Aquino, K., Kia, S.M., Wolfers, T., Franke, B., Hoogman, M., Beckmann, C.F., Westlye, L.T., Andreassen, O.A., Zalesky, A., Harrison, B.J., Davey, C.G., Soriano-Mas, C., Cardoner, N., Tiego, J., Yücel, M., Braganza, L., Suo, C., Berk, M., Cotton, S., Bellgrove, M.A., Marquand, A.F., Fornito, A., 2023. Nat. Neurosci. 26, 1613–1629. https://doi.org/10.1038/s41593-023-01404-6.
- Stosiek, C., Garaschuk, O., Holthoff, K., Konnerth, A., 2003. Proc. Natl. Acad. Sci. 100, 7319–7324. https://doi.org/10.1073/pnas.1232232100.
- Sulzer, D., 2011. https://doi.org/10.1016/j.neuron.2011.02.010.
- Surmeier, D.J., Ding, J., Day, M., Wang, Z., Shen, W., 2007. https://doi.org/10.1016/j. tins.2007.03.008.
- Sych, Y., Chernysheva, M., Sumanovski, L.T., Helmchen, F., 2019. Nat. Methods 16, 553–560. https://doi.org/10.1038/s41592-019-0400-4.
- Toda, H., Suzuki, T., Sawahata, H., Majima, K., Kamitani, Y., Hasegawa, I., 2011.
 Neuroimage 54, 203–212. https://doi.org/10.1016/j.neuroimage.2010.08.003
- Todaro, C., Marzetti, L., Valdés Sosa, P.A., Valdés-Hernandez, P.A., Pizzella, V., 2019. Brain Topogr. 32, 583–598. https://doi.org/10.1007/s10548-018-0623-1.
- Tort-Colet, N., Resta, F., Montagni, E., Pavone, F., Allegra Mascaro, A.L., Destexhe, A., 2023. Sci. Rep. 13, 3183. https://doi.org/10.1038/s41598-023-30224-8.
- Vázquez-Guardado, A., Yang, Y., Bandodkar, A.J., Rogers, J.A., 2020. Nat. Neurosci. 23, 1522–1536. https://doi.org/10.1038/s41593-020-00739-8.
- Wandell, B.A., Le, R.K., 2017. Neuron. https://doi.org/10.1016/j.neuron.2017.08.007.
- Wei, Z., Lin, B.-J., Chen, T.-W., Daie, K., Svoboda, K., Druckmann, S., 2020. PLoS Comput. Biol. 16, e1008198. https://doi.org/10.1371/journal.pcbi.1008198.
 Yasaka, K., Kamagata, K., Ogawa, T., Hatano, T., Takeshige-Amano, H., Ogaki, K.,
- Andica, C., Akai, H., Kunimatsu, A., Uchida, W., Hattori, N., Aoki, S., Abe, O., 2021. Neuroradiology. https://doi.org/10.1007/s00234-021-02648-4/Published.
- Zátonyi, A., Borhegyi, Z., Srivastava, M., Cserpán, D., Somogyvári, Z., Kisvárday, Z., Fekete, Z., 2018. Sensors Actuators, B Chem. 273, 519–526. https://doi.org/ 10.1016/j.snb.2018.06.092.
- Zhang, J., Liu, X., Xu, W., Luo, W., Li, M., Chu, F., Xu, L., Cao, A., Guan, J., Tang, S., Duan, X., 2018. Nano Lett. 18, 2903–2911. https://doi.org/10.1021/acs. nanolett.8b00087.
- Zhang, Y., Yuan, L., Zhu, Q., Wu, J., Nöbauer, T., Zhang, R., Xiao, G., Wang, M., Xie, H., Guo, Z., Dai, Q., Vaziri, A., 2024. Nat. Biomed. Eng. 8, 754–774. https://doi.org/ 10.1038/s41551-024-01226-2.